

Depth-segmented detector for x-ray absorptiometry

Grant M. Stevens and Norbert J. Pelc

Departments of Radiology and Applied Physics, Stanford University, Stanford, California 94305

(Received 6 August 1999; accepted for publication 6 February 2000)

A new energy-dependent multi-cell detector, which is a generalization of the conventional front-back detector, was studied using computer simulations. The noise performance of the detector for bone quantitation was examined in comparison to an ideal energy discriminating detector, and front-back detectors with and without inter-detector filters. The front-back detectors were optimized for a reference object composed of water and bone, and then compared to the new detector over a range of object compositions. In this paper, precision in calculated bone thickness is used as the criterion for evaluating detector performance. Simulations show that the segmented detector always performs better than the front-back detector without an inter-detector filter. It outperforms the detector incorporating a filter by an amount that depends on the heterogeneity of the x-ray spectrum. In addition, for single component radiographic images, this multi-cell detector retains information which is lost in the front-back detector with a filter layer. © 2000 American Association of Physicists in Medicine. [S0094-2405(00)01405-X]

Key words: DEXA, bone quantitation

I. INTRODUCTION

X-ray measurements at two energies can be used for selective material imaging.¹ While applications such as imaging of chest² and breast³ have been explored, the most common use for this type of imaging is in the quantitative measurement of bone. Dual energy x-ray absorptiometry is the dominant bone measurement technique in the US.⁴ With the recent FDA approval of new drugs for treating the loss in bone resulting from osteoporosis, interest in performing bone mineral measurements has been strengthened.⁵⁻⁷

Dual energy imaging can be performed using monoenergetic sources, such as radionuclides. This can lead to motion artifacts during the long scan times required or poor precision in the images, due to the low output of the sources. Alternatively, high output monoenergetic sources can be approximated by using kV-switched x-ray tubes with appropriate filtration.⁸ While this method is viable, it is technically complex. A single x-ray exposure can be used with a front-back detector, and its performance can be improved with the incorporation of a filter layer between the two cells.⁹⁻¹⁴ While this method is simpler to implement, its precision is inferior to that of the dual kVp approach for the same dose.¹⁵

Alternatively, consider a detector in which the energy deposited could be measured as a function of depth in the detector. Information about the spectrum of the x-ray beam would be extracted from the signal as a function of depth. This is essentially a generalization of the front-back detector. We hypothesized that this detector would outperform the front-back detector, both with and without an inter-detector filter.

In addition to making "material selective" images, multi-energy imaging systems may be called upon to generate "radiographic" images.¹² For example, dual energy x-ray absorptiometry (DEXA) systems yield not only images and quantitation of bone mineral using dual energy subtraction,

but also high SNR single energy anatomic images. Therefore, this mode was included in our evaluation of the relative performance of the multi-cell detector.

In this paper, we report the results of computer simulations which compare the precision in quantitating bone using front-back detectors, with and without a filter, and the multi-cell detector. X-ray measurements are simulated for a range of tissue and bone thicknesses, and the resulting bone precision is determined. In order to provide a reference for these comparisons, a perfect energy-discriminating detector is simulated as an ideal detector.

II. MOTIVATION

A. Two cell detector

Consider the case of an x-ray beam containing photons of two energies incident on a front-back detector. The detector signals from the two cells are:

$$S_F = \alpha_1 \eta_{F1} N_1 + \alpha_2 \eta_{F2} N_2, \quad S_B = \alpha_1 \eta_{B1} N_1 + \alpha_2 \eta_{B2} N_2. \quad (1)$$

Here, S_F is the signal from the front cell, and S_B is the signal from the back cell. The detection efficiency for the front cell at energy E_j ($j=1, \dots, 2$) is η_{Fj} , and η_{Bj} is the detection efficiency for the back cell at energy E_j . Note that the back cell efficiencies include the effect of the x-rays absorbed in the front cell. The term α_j is a constant which has value 1 for a photon-counting detector and value equal to the energy, E_j , for an intensity-based detector. N_1 and N_2 are the expected number of x-rays of energy E_1 and E_2 transmitted through the body.

From the signals given in Eq. (1), the number of x-rays transmitted through the body at each of the two energies can be obtained:

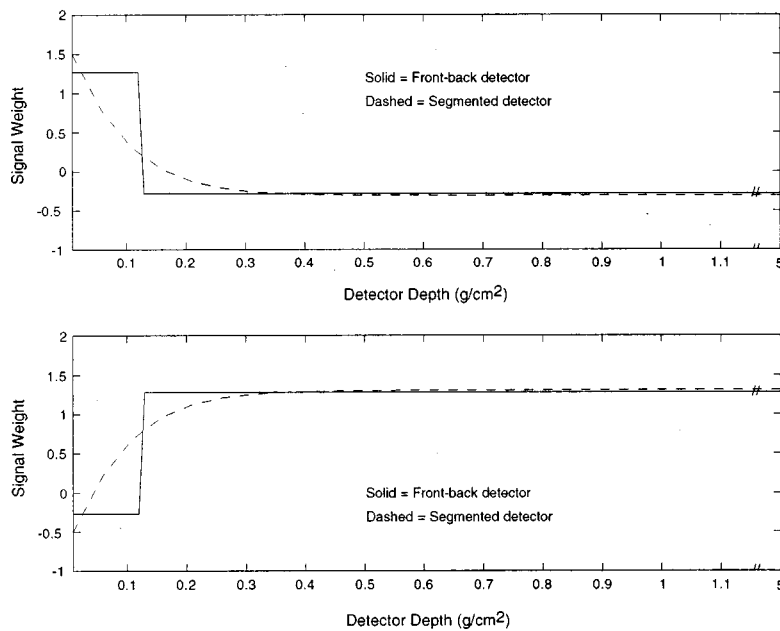


FIG. 1. Weighting functions of a two cell detector (solid) and a segmented detector (dashed) for the calculation of intensity at each energy in a dual energy spectrum. The top subplot shows the weights to generate the low energy signal and the bottom subplot shows the high energy weights. In this example, the detector is NaI, the two energies are 44 and 100 keV, and $\alpha_j = E_j$.

$$N_1 = \left(\frac{1}{\alpha_1} \right) \left(\frac{\eta_{B2} S_F - \eta_{F2} S_B}{\eta_{F1} \eta_{B2} - \eta_{F2} \eta_{B1}} \right), \quad (2)$$

$$N_2 = \left(\frac{1}{\alpha_2} \right) \left(\frac{-\eta_{B1} S_F + \eta_{F1} S_B}{\eta_{F1} \eta_{B2} - \eta_{F2} \eta_{B1}} \right).$$

Thus, the number of photons at each energy in Eq. (2) can be expressed as a weighted sum of the front and back detector cell signals:

$$N_1 = f_{F1} S_F + f_{B1} S_B, \quad N_2 = f_{F2} S_F + f_{B2} S_B. \quad (3)$$

In Eq. (3), the weighting functions, f_{F1} , f_{F2} , f_{B1} , and f_{B2} , are easily obtained by examination of Eq. (2). Photons detected in the front cell are weighted by f_{F1} and f_{F2} regardless of where in the front cell they are detected. Similarly, photons contributing to the back cell signal are weighted by f_{B1} and f_{B2} . Thus, we can interpret the contribution of photons detected at various depths in the detector as shown graphically in Fig. 1 for a representative design. Because most of the low energy x-rays are absorbed in the front cell while most of the high energy x-rays penetrate to the back cell, the low energy intensity (N_1 , the top subplot in Fig. 1) is largely from the front cell. A small amount of the back cell signal is subtracted, as noted by the negative weighting, in order to remove the effect of high energy x-rays absorbed in the front detector. Likewise, the high energy intensity (N_2) has a small negative weighting for the front cell signal. The weightings as functions of depth are discontinuous at the boundary between the front and back cells. From this, we expect that signal generated near the boundary is not being optimally utilized, and that segmenting the detector more finely in depth could be beneficial.

B. Multi-cell detector

A derivation similar to that above can be made for a detector which is segmented into N cells along the path of the incident x-rays. The detector signals from each of the N cells are:

$$S_i = \alpha_1 \eta_{i1} N_1 + \alpha_2 \eta_{i2} N_2, \quad i = 1 \dots N. \quad (4)$$

Here, η_{ij} is the detector efficiency of cell i at energy E_j , which includes the effect of the cells in front of the i th cell; while N_j and α_j are as before. Equation (4) can be solved for the number of low and high energy x-rays as weighted functions of the cell signals, as was done above for the two cell case. Since the system of equations is overdetermined, in order to solve this in the general N cell case, a weighted least squares approach is used. The weighted sum of the squared differences between the measured signal and the modeled signal given [Eq. (4)] is:

$$\chi^2 = \sum_{i=1}^N [\tilde{S}_i - \alpha_1 \eta_{i1} N_1 - \alpha_2 \eta_{i2} N_2]^2 w_i. \quad (5)$$

Here, \tilde{S}_i is the measured signal from the i th cell, and w_i is a weighting factor. For optimal SNR, the ideal choice for w_i is the inverse of the variance of \tilde{S}_i ,¹⁶ which can be approximated by the inverse of the variance of the modeled signal. Setting the partial derivatives of Eq. (5) with respect to N_1 and N_2 equal to zero and solving for the number of low and high energy x-rays as weighted sums of the detector signals yields:

$$N_j = \sum_{i=1}^N f_{ij} \tilde{S}_i, \quad j = 1, 2, \quad (6)$$

where

$$f_{ij} = \frac{w_i}{\alpha_j} \frac{(\sum_{k=1}^N \eta_{k,3-j}^2 w_k) \eta_{ij} - (\sum_{k=1}^N \eta_{k1} \eta_{k2} w_k) \eta_{i,3-j}}{(\sum_{k=1}^N \eta_{k1}^2 w_k)(\sum_{k=1}^N \eta_{k2}^2 w_k) - (\sum_{k=1}^N \eta_{k1} \eta_{k2} w_k)^2}. \quad (7)$$

As the number of cells increases, the weighting functions in Eq. (7) more closely approximate continuous functions. Example weighting functions for a 100 cell detector are shown in Fig. 1. As expected, the low energy signal is derived mainly from the front region of the detector, with a negative weighting for the deeper cells. A detector with only two cells is hindered because it must use a constant weighting over a range of detector depths in which the optimal weighting changes significantly. A detector which is segmented into more cells is better able to accommodate the region of the detector where comparable number of low and high energy x-rays are absorbed. An additional advantage of the multi cell detector is its flexibility to adapt to changes in the spectral composition due either to hardening of the beam or changes in the technique. The front-back detector is unable to adapt to these changes. This simple derivation shows the increased flexibility of the multi-cell detector, which can more finely differentiate the regions of x-ray absorbance in the detector.

III. METHODS

A. Bone imaging

We derive first the well-known relationship for dual monoenergetic imaging and then generalize for polychromatic beams. Use of more than two energies is then studied.

1. Two energy measurements

Given the motivation of how detectors record energy-dependent signals, consider the task of extracting the thickness of bone in the object from the detector signals. The simplest conceptual approach to this problem is to use two single energy measurements (i.e., each measurement is sensitive to photons of only a single energy). As is well known, this could be achieved, for example, by two successive measurements of two monoenergetic beams incident on a single cell detector. The amount of bone present is a simple linear combination of the log signals at the two energies, L_1 and L_2 :

$$B = \frac{\mu_{w2} L_1 - \mu_{w1} L_2}{\mu_{w2} \mu_{B1} - \mu_{w1} \mu_{B2}}. \quad (8)$$

Here, L_j is the logarithm of the ratio of the radiation incident on the body to the radiation transmitted through the body, and μ_{wj} and μ_{Bj} represent the energy-dependent linear attenuation coefficients of water and bone, respectively. The numerical subscripts denote energy, and B is the thickness of bone (alternatively, one can use mass attenuation coefficients to compute bone mass per unit area). The expected noise in the calculated bone can be derived using propagation of errors. Assuming the measurements have uncorrelated noise, the expected noise is:

$$\sigma_B^2 = \sum_{j=1}^2 \left(\frac{\partial B}{\partial L_j} \right)^2 \left(\frac{\partial L_j}{\partial S_j} \right)^2 \sigma_{S_j}^2 = \frac{\mu_{w2}^2 \alpha_1 S_2 + \mu_{w1}^2 \alpha_2 S_1}{S_1 S_2 (\mu_{w2} \mu_{B1} - \mu_{w1} \mu_{B2})^2}. \quad (9)$$

S_j is the detector signal at energy E_j , which has a variance of $\alpha_j S_j$. Inherent in Eq. (9) is the assumption that the incident intensity is well known from prior measurements, or is relatively noiseless. If this is not the case, a more general form of Eq. (9) can account for the additional noise source.

In the case of DEXA measurements using x-ray tubes, the spectra are broader. Because of this, the signal equations are not as easy to linearize. Normally, linearization is performed using beam hardening corrections such as a polynomials in the log signals. Because our criterion for comparing detector systems is noise in quantitated bone, we will use a simpler approach. We seek to quantify the effect of signal fluctuation due to quantum noise on the measured amount of bone. We allow the system to operate differentially about a reference operating point, which is the expected value of tissue and bone. The detector signals are expressed as these reference signals modified by attenuation through additional small amounts of water and bone. Over a small range of thicknesses, attenuation of the polychromatic beam can be approximated as exponential, characterized by the effective attenuation coefficients for bone and water, which are defined as:

$$\bar{\mu}_{Bi} = -\frac{\partial S_i}{\partial \delta B}, \quad \bar{\mu}_{wi} = -\frac{\partial S_i}{\partial \delta W}. \quad (10)$$

For small δB and δW , the two DEXA signals can be approximated as:

$$S_i = \left(\sum_{j=1}^M N_j^{\text{ref}} \alpha_j \eta_{ij} \right) e^{-\bar{\mu}_{Bi} \delta B - \bar{\mu}_{wi} \delta W}, \quad i = 1, \dots, 2. \quad (11)$$

Here, N_j^{ref} is the expected number of x-rays to penetrate through the reference amount of tissue and bone at energy E_j , and M is the number of energy bins in the discretized x-ray spectrum. Equation (11) can be solved directly for the incremental amount of bone:

$$\delta B = \frac{\bar{\mu}_{w2} \ln \left(\frac{S_1^{\text{ref}}}{S_1} \right) - \bar{\mu}_{w1} \ln \left(\frac{S_2^{\text{ref}}}{S_2} \right)}{\bar{\mu}_{B1} \bar{\mu}_{w2} - \bar{\mu}_{w1} \bar{\mu}_{B2}}, \quad (12)$$

where S_j^{ref} is the signal with δB and δW equal to zero. The variance, as proven by Morgan,¹² is:

$$\sigma_B^2 = \frac{\bar{\mu}_{w2}^2 S_2^2 (\sum_{j=1}^M N_j \alpha_j^2 \eta_{1j}) + \bar{\mu}_{w1}^2 S_1^2 (\sum_{j=1}^M N_j \alpha_j^2 \eta_{2j})}{(S_1 S_2)^2 (\bar{\mu}_{B1} \bar{\mu}_{w2} - \bar{\mu}_{w1} \bar{\mu}_{B2})^2}, \quad (13)$$

where each signal has variance $\sum_{j=1}^M N_j \alpha_j^2 \eta_{ij}$. In Eq. (12), δB can also be interpreted as the fluctuation in the computed bone due to the fluctuation of the measured signals (S_j) about the expected values (S_j^{ref}). Equations (12) and (13) reduce to Eqs. (8) and (9) in the case of two separate energy measurements ($M = 2$, $\eta_{12}, \eta_{21} = 0$), with the attenuation co-

efficients replaced by effective attenuation coefficients. Numerical simulations were performed and validated the accuracy of this approach to calculate the noise in measured bone thickness. Equation (13) can be used to calculate the variance in computed bone for techniques that use two polyenergetic measurements, such as dual kV DEXA or measurements with a front-back detector.

2. More than two energy measurements

To analyze the performance of the proposed multi-cell detector, we need to develop a method to calculate the amounts of tissue and bone given more than two energy measurements. A detailed derivation of the equations in this section is given in the Appendix. Suppose that measurements

with more than two energies are available, e.g., for an energy-discriminating detector and an x-ray spectrum containing M different energies. For $M > 2$, the problem of quantitating a two-component mixture (i.e., bone and water) is overdetermined. A weighted least squares solution may be employed to optimally solve for the amount of bone present. The log of the x-ray transmission at each energy is related to the amount of bone and water. We solve for the amounts of bone and water that minimize the weighted sum of the squared difference between the actual log measurements and the expected values for a given amount of bone and tissue. The optimal weights are the inverse of the log signal variances, as previously noted. The weighted least squares solution for the amount of bone is:

$$B = \frac{(\sum_{j=1}^M \mu_{Wj}^2 w_j)(\sum_{j=1}^M \mu_{Bj} L_j w_j) - (\sum_{j=1}^M \mu_{Bj} \mu_{Wj} w_j)(\sum_{j=1}^M \mu_{Wj} L_j w_j)}{(\sum_{j=1}^M \mu_{Bj}^2 w_j)(\sum_{j=1}^M \mu_{Wj}^2 w_j) - (\sum_{j=1}^M \mu_{Bj} \mu_{Wj} w_j)^2}. \quad (14)$$

For the two energy case ($M=2$, $w_1, w_2=1$), Eq. (14) reduces to Eq. (8), as expected. As before, one may calculate the expected noise in the measured bone:

$$\sigma_B^2 = \sum_{n=1}^M \left[\frac{(\sum_{j=1}^M \mu_{Wj}^2 w_j) \mu_{Bn} w_n - (\sum_{j=1}^M \mu_{Bj} \mu_{Wj} w_j) \mu_{Wn} w_n}{(\sum_{j=1}^M \mu_{Bj}^2 w_j)(\sum_{j=1}^M \mu_{Wj}^2 w_j) - (\sum_{j=1}^M \mu_{Bj} \mu_{Wj} w_j)^2} \right]^2 \frac{\alpha_n}{S_n}. \quad (15)$$

As before, the variance in each signal is $\alpha_n S_n$.

Equations (14) and (15) describe the case of M monoenergetic measurements. For the case in which we have more than two polychromatic measurements, we replace the attenuation coefficients with effective attenuation coefficients and operate about a reference amount of bone and tissue:

$$\delta B = \frac{(\sum_{i=1}^K \bar{\mu}_{Wi}^2 w_i)(\sum_{i=1}^K \bar{\mu}_{Bi} L_i w_i) - (\sum_{i=1}^K \bar{\mu}_{Bi} \bar{\mu}_{Wi} w_i)(\sum_{i=1}^K \bar{\mu}_{Wi} L_i w_i)}{(\sum_{i=1}^K \bar{\mu}_{Bi}^2 w_i)(\sum_{i=1}^K \bar{\mu}_{Wi}^2 w_i) - (\sum_{i=1}^K \bar{\mu}_{Bi} \bar{\mu}_{Wi} w_i)^2}. \quad (16)$$

Here, K refers to the number of polychromatic measurements, while M is still the number of energies in the spectrum. L_i is the logarithm of the ratio of the expected signal for the reference amount of bone and tissue to the i th measured signal. From this, the variance in the computed bone can be analytically predicted:

$$\sigma_B^2 = \sum_{n=1}^K \left[\frac{(\sum_{i=1}^K \bar{\mu}_{Wi}^2 w_i) \bar{\mu}_{Bn} w_n - (\sum_{i=1}^K \bar{\mu}_{Bi} \bar{\mu}_{Wi} w_i) \bar{\mu}_{Wn} w_n}{(\sum_{i=1}^K \bar{\mu}_{Bi}^2 w_i)(\sum_{i=1}^K \bar{\mu}_{Wi}^2 w_i) - (\sum_{i=1}^K \bar{\mu}_{Bi} \bar{\mu}_{Wi} w_i)^2} \right]^2 \frac{1}{S_n^2} \sum_{j=1}^M N_j \alpha_j^2 \eta_{nj}. \quad (17)$$

As before, the variance in each signal is $\sum_{j=1}^M N_j \alpha_j^2 \eta_{ij}$. We stress here that with a single effective attenuation coefficient at each measurement, Eq. (16) may not be accurate over a wide dynamic range and beam hardening corrections may be needed. However, Eq. (17) can still be used to predict the noise performance for bone quantitation.

B. Radiographic imaging

When generating a ‘‘radiographic’’ image, we are mainly interested in the ability to form a single ‘‘anatomic’’ image from all the energy measurements, and we are particularly interested in the ability of this image to portray subtle details in the bone present. Consider a small region of the image over which we can consider the total thickness to be relatively constant. We want to examine the ability of a single

combined image to depict a small change T in the thickness of bone. For a single energy measurement, the expected signal can be expressed as:

$$S_T = S^{\text{ref}} e^{-(\mu_B - \mu_W)T}. \quad (18)$$

Here, S^{ref} is the signal for the reference operating point, and T is the incremental thickness of water replaced by bone. The monoenergetic x-ray measurement of T using Eq. (18) has a variance of:

$$\sigma_T^2 = \frac{\alpha}{S_T (\mu_B - \mu_W)^2}, \quad (19)$$

where α is the signal per photon. For a single polychromatic measurement, the attenuation coefficients in Eqs. (18) and (19) would be replaced by effective attenuation coefficients.

If more than one energy measurement is available, the problem is overdetermined. That is, a radiograph can be formed at each energy and we seek the ideal combination of these. These multiple measurements could result from detecting more than one monoenergetic beam or from using segmented detectors to make multiple measurements of a polychromatic spectrum. For monoenergetic x-rays, each photon energy produces a signal of the form given by Eq. (18) and therefore an estimate of T . Using the same optimization methodology as before, the minimum least squares linear combination of these is:

$$T = \frac{\sum_{i=1}^K L_i (\mu_{Bi} - \mu_{Wi}) w_i}{\sum_{i=1}^K (\mu_{Bi} - \mu_{Wi})^2 w_i}. \quad (20)$$

L_i is the log signal relative to the reference amount of tissue and bone, and K is the number of measurements. As before, the optimal weights are the inverse of the log signal variances. Each signal S_n has variance $\alpha_n S_n$. The variance in the estimated value of T is:

$$\sigma_T^2 = \sum_{n=1}^K \frac{\alpha_n [(\mu_{Bn} - \mu_{Wn}) w_n]^2}{S_n [\sum_{i=1}^K (\mu_{Bi} - \mu_{Wi})^2 w_i]^2}. \quad (21)$$

Equation (20) describes how the multiple single energy radiographic images should be combined, and Eq. (21) is a measure of the image quality (variance) to be expected.

For multiple polychromatic measurements (e.g., with a depth segmented detector), Eqs. (20) and (21) hold with slight modifications. The attenuation coefficients are replaced by effective attenuation coefficients, and the signals have variances $\sum_{j=1}^M N_j \alpha_j^2 \eta_{nj}$ (M denotes the number of energy bins in the discretized spectrum). Thus, for a polychromatic beam:

$$T = \frac{\sum_{i=1}^K L_i (\bar{\mu}_{Bi} - \bar{\mu}_{Wi}) w_i}{\sum_{i=1}^K (\bar{\mu}_{Bi} - \bar{\mu}_{Wi})^2 w_i} \quad (22)$$

and

$$\sigma_T^2 = \sum_{n=1}^K \frac{[(\bar{\mu}_{Bn} - \bar{\mu}_{Wn}) w_n]^2 \sum_{j=1}^M N_j \alpha_j^2 \eta_{nj}}{S_n [\sum_{i=1}^K (\bar{\mu}_{Bi} - \bar{\mu}_{Wi})^2 w_i]^2}. \quad (23)$$

C. Simulations

The algorithms described in Secs. III A and III B were employed in computer simulations to model system performances over a range of body compositions. The systems simulated were: (1) a perfect energy-discriminating system, (2) a front-back detector with and (3) without an inter-detector filter, and (4) a multi-cell detector. In these simulations, the total thickness of the detectors was chosen to be 5 g/cm² of NaI, as in Kelcz *et al.*¹⁵ This total thickness was divided into segments of unequal thickness for the front-back detectors, and into 100 uniformly sized cells for the segmented detector proposed in this paper. While a detector segmented into this many cells may not be practical, a 100 cell design was used in order to study the maximum possible benefit of depth segmentation of the type envisioned here.

Unless otherwise mentioned, the detectors were assumed to be intensity-based ($\alpha_j = E_j$). The attenuation coefficients for the detector, filters, and tissues used for the calculations are from NIST.¹⁷ The bone attenuation coefficient was based on cortical bone (% by weight: 3.4% H, 15.5% C, 4.2% N, 43.5% O, 0.1% Na, 0.2% Mg, 10.3% P, 0.3% S, 22.5% Ca).¹⁸ The simulations were run for a range of bone (0.8–1.8 cm) and water (15–25 cm) thicknesses. A density of 1.65 g/cm³ was assumed for bone, and a density of 1.04 g/cm³ for water (to mimic muscle tissue).¹⁹ Simplifying assumptions of no scatter and no cross-talk between cells in the detectors were made in order to carry out the noise analysis. All analytical algorithms were verified using numerical simulations.

A two monochromatic energy simulation was run using a spectrum containing x-rays at 44 keV and 100 keV, modeling the emissions of ¹⁵³Gd. The ratio of the incident intensities at the two energies was optimized for the front-back detector without a filter, keeping the total number of x-rays fixed. Alternatively, one could choose this ratio by holding the dose constant, but this should not greatly change the comparison among systems for this simple case. The segmentation into front and back cells was optimized to minimize the variance in the measured amount of bone for an object composed of 1.3 cm of bone and 20 cm of water, keeping the total detector thickness fixed. This optimization yielded a ratio of 18:1 low to high energy x-rays, and front and back cells of 0.12 g/cm² and 4.88 g/cm², respectively, for the front-back detector without an inter-detector filter. For the front-back with a filter, the filter material was assumed to also be NaI, as in Cardinal and Fenster where the filter layer was composed of the same material as the detector.¹⁰ Part of the total 5 g/cm² of the detector was assigned to be the filter (i.e., the filter is essentially an inactive NaI cell). The optimal apportionment of the total thickness was 0.08 g/cm² for the front cell, 0.11 g/cm² for the filter, and 4.81 g/cm² for the back cell.

Simulations were also run for photon counting detectors ($\alpha_j = 1$). The ratio of x-rays was re-optimized, yielding a ratio of 8.7:1 low to high energy x-rays. Optimal cell sizes were 0.15 g/cm² for the front cell and 4.85 g/cm² for the back cell for the front-back detector with no filter, and 0.10 g/cm² for the front cell, 0.12 g/cm² for the filter, and 4.78 g/cm² for the back cell for the front-back detector with a filter.

Polychromatic beam simulations were run using a 150 kVp beam filtered with 1 mm Al (to model inherent filtration) and an additional 0.17 mm Hf (as in Cardinal and Fenster¹⁰). The Hf filtration is beneficial because hafnium, with a K-edge at 65.35 keV, produces a bimodal spectrum. The spectrum was calculated using in-house software based on theory by Storm *et al.*²⁰ and data from Dyson,²¹ and is shown in Fig. 2. For this polychromatic spectrum, the optimal cell sizes were 0.23 g/cm² and 4.77 g/cm², respectively for the front-back detector without a filter, and 0.16 g/cm², 0.30 g/cm², and 4.54 g/cm² for the front-back detector with a filter. The cell sizes were not re-optimized for the construction of a radiographic image [Eq. (20)], as the goal was to compare the image noise from detectors optimized for quan-

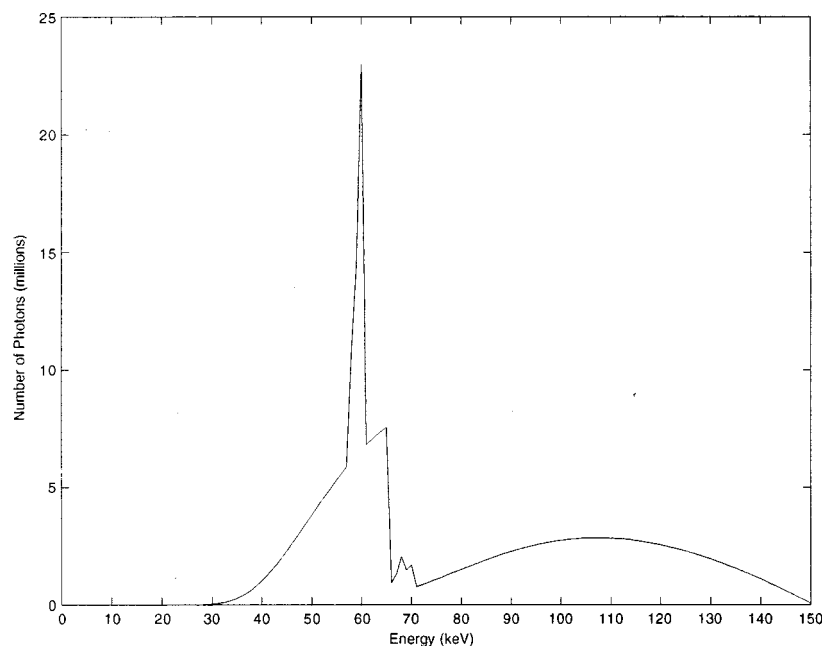


FIG. 2. X-ray spectrum used in polychromatic bone imaging and radiographic imaging (150 kVp beam with 1 mm Al and 0.17 mm Hf filtration).

titative bone measurements. We also considered a system with photon counting front-back detectors. The optimal cell sizes for this configuration were 0.26 g/cm^2 for the front cell and 4.74 g/cm^2 for the back cell for the front-back detector with no filter, and 0.16 g/cm^2 for the front cell, 0.31 g/cm^2 for the filter, and 4.53 g/cm^2 for the back cell for the front-back detector with a filter.

For each of the simulations, the predicted standard deviation in the thickness of bone was calculated. This standard deviation was used to compare the expected performance of each of the detector systems. The precision at the optimization point was used to compare how well each detector works at its optimal performance. Examination of the results away from the optimization point allows a comparison of how the detectors perform relative to one another as the bone and water thicknesses move away from the design point. This demonstrates the relative flexibility of the detectors for use with different patients. In addition, a perfect energy-discriminating detector of the same overall thickness was simulated to be used as an ideal detector for comparison. In the case of polychromatic simulations, the signals from this ideal detector were combined optimally using the weighted least squares technique.

IV. RESULTS

A. Dual energy bone imaging

Simulations using a dual energy spectrum (44 and 100 keV) show all of the segmented detectors to be significantly poorer than the ideal system (which has perfect energy separation). Figure 3 shows the noise performance of the front-back detector without a filter layer relative to the ideal energy-discriminating detector. From our simulations, the performance of the front-back detector can be improved by around 5% by the addition of the inactive filter layer. The improvement afforded by the addition of the filter layer was

roughly uniform over the range of composition, ranging from 4.2% at 1.25 cm bone, 15 cm water to 5.0% at 1.80 cm bone, 25 cm water. The segmented detector achieves an additional 2%–3% gain over the two cell detector with an intradetector filter, the greatest improvements being for thicker objects. These improvements are summarized in Table I.

B. Polychromatic bone imaging

In the case of a polychromatic beam, the performance of the two cell detector is even further from the ideal detector. Figure 4 shows that the intensity-based front-back detector without a filter yields a calculated bone thickness that has a standard deviation of approximately three times that of the equivalent measurement by a perfect energy-discriminating detector. An improvement of just over 6% can be made with the addition of an inactive filter layer. This improvement is quite homogeneous, ranging from 6.0% at 0.80 cm bone, 15 cm water to 6.4% at 1.80 cm bone, 20.0 cm water. An additional 5% gain can be achieved by using the segmented detector. Table I summarizes the improvements for polychromatic bone imaging.

For all detector types (except the ideal energy discriminating detector), the photon counting mode ($\alpha_j = 1$) is superior to the intensity mode ($\alpha_j = E_j$). For example, for bone quantitation with a front-back detector with no filter and a polychromatic beam, photon counting reduces the standard deviation by about 30%. For this system, use of an inter-detector filter provides an additional 6% improvement, as is summarized in Table II. The segmented detector provides an additional improvement of 4%–5% as compared to the front-back detector with a filter. Thus, the improvement provided by the segmented detector is slightly larger in an intensity detector than in photon counting mode.

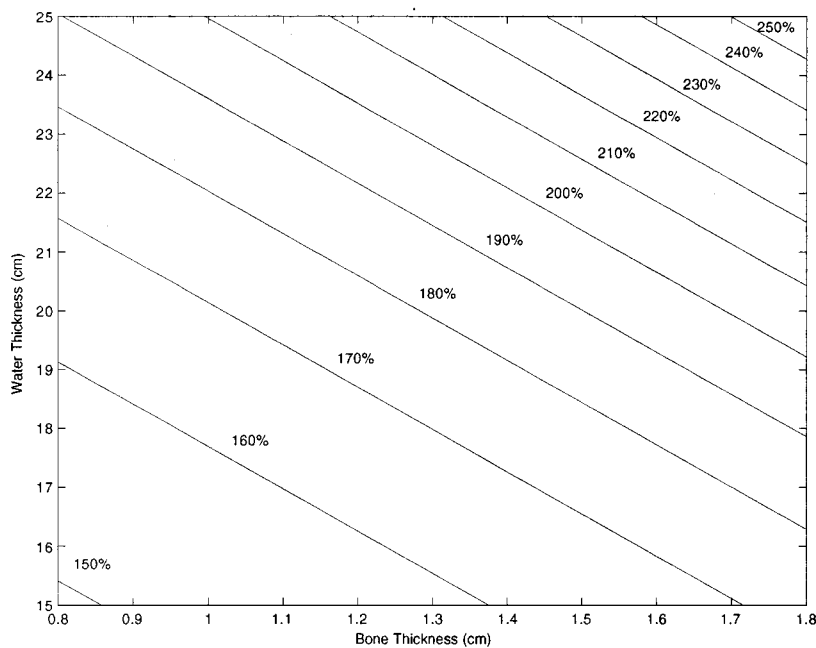


FIG. 3. Standard deviation in computed bone for the two cell detector relative to the ideal energy discriminating detector, for a two energy x-ray beam. The numerical values on the plot correspond to the contour lines to the left of the numbers. A value of 100% indicates equal standard deviations for the two cell detector and the ideal detector.

C. Radiographic imaging

For constructing a single radiographic image from multiple measurements, the depth discriminating detectors no longer perform as poorly as compared to the ideal energy-discriminating detector. Shown in Fig. 5 is the standard deviation for a front-back detector relative to the ideal detector for a polychromatic beam. This figure shows that the two cell detector without a filter is only 20%–28% noisier than the ideal system. In the case of the front-back detector with a filter, the loss of information from wasting photons absorbed in the filter results in a further increase in noise of 16%–17% throughout the range of water and bone thicknesses. The segmented detector, which retains these photons, yields a 1% improvement over the front-back detector without a filter and a 15% improvement over the front-back detector with a filter.

V. DISCUSSION

Our dual energy simulations show all of the segmented detectors to be far inferior to the ideal system because of their incomplete energy separation. It can be seen in Figs. 3 and 4 that the relative performance worsens as a function of the total body thickness. All of the detectors behave similarly in this regard, and results from a shift in the x-ray spectrum incident on the detector due to beam hardening. As the total thickness increases, a higher percentage of high energy

x-rays are retained in the beam and the signal from the front cell is increasingly less representative of a low energy measurement. The situation is further worsened for the two cell detectors because of their fixed cell size. Ideally, as the beam becomes richer in high energy photons, one should reduce the thickness of the front cell. These fixed systems, however, are unable to shrink the front cell size to counteract the larger proportion of high energy x-rays in the beam.

Our simulations demonstrate an improvement of around 6% for a two cell detector by the addition of an inactive filter layer. This is in agreement with previously published results on two cell detectors. Cardinal and Fenster¹⁰ demonstrated an improvement of 6%–7% for a similar attenuating object and filtered spectrum. Kelcz *et al.*¹⁵ showed an improvement of 3%–4% in high Z compounds, Gauntt and Barnes¹³ showed an improvement of 4%–6% for various object compositions, and Chakraborty and Barnes¹⁴ showed an improvement of around 4% for a theoretical mammography setup.

A main purpose of our study was to evaluate whether a more finely segmented detector could improve on this performance. For a simple dual energy spectrum, the additional improvement in the standard deviation of bone provided by using a segmented detector is modest as compared to a front-back detector with a filter. For a polychromatic beam, the additional improvement in bone quantitation provided by the segmented detector over a front-back detector with a filter is larger than for the simple dual energy spectrum, and is significant. This suggests that the use of a filter is not as efficient at removing spectral overlap in this more complex case. All the divided detectors (i.e., front-back detectors with and without a filter, and the segmented detector) are hindered when used with polychromatic spectra because of the inherent averaging over energy which takes place in each cell.

TABLE I. Reductions in standard deviation in the measured bone as compared to a front-back detector for the front-back detector with a filter and for the multi-cell detector, for the dual energy and polychromatic cases.

Spectrum	Front-back with filter	Segmented
44 and 100 keV	4.2%–5.0%	6.0%–8.1%
150 kVp, 1 mm Al, 0.17 mm Hf	6.0%–6.4%	10.4%–11.5%

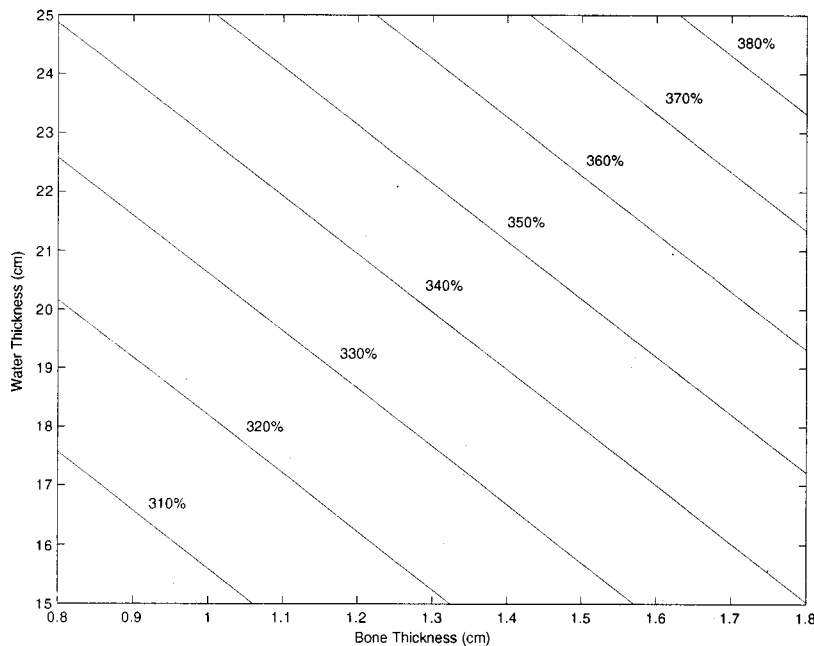


FIG. 4. Standard deviation in computed bone for the two cell detector relative to the ideal energy discriminating detector, for a filtered 150 kVp beam. The numerical values on the plot correspond to the contour lines to the left of the numbers. A value of 100% indicates equal standard deviations for the two cell detectors and the ideal detector.

In the additional role of using multiple measurements to construct a single “radiographic” image, the main factor in image quality is the number of x-rays absorbed in the detector. For this case, the depth discriminating detectors no longer perform as poorly as compared to the ideal energy-discriminating detector. Because the front-back detector with a filter wastes photons absorbed in the filter layer, the system has higher noise throughout the range of water and bone thicknesses. Thus, the use of a filter to increase the performance of a two cell detector for bone quantitation comes at the cost of increased noise in “radiographic” images. Because these photons are still available in the segmented detector system, they can be used to generate a less noisy image. This demonstrates the increased flexibility of the multi cell detector.

As part of our study, we derived an algorithm to measure the composition of a two component system (e.g., tissue and bone) from more than two energy measurements [Eqs. (14) and (16)]. The derivation was motivated by the need to use the data from the segmented detector, but the method may find more utility in other systems, for example with pulse height analysis.

TABLE II. Reductions in standard deviation in the measured bone as compared to a intensity-based front-back detector for the photon counting front-back detector without a filter, for the photon counting front-back detector with a filter, and for the photon counting multi-cell detector for the dual energy and polychromatic cases.

Spectrum	Front-back	Front-back with filter	Segmented
44 and 100 keV	22.8%–26.5%	26.3%–30.4%	27.7%–32.6%
150 kVp, 1 mm Al,	27.0%–32.9%	31.6%–37.2%	34.5%–40.3%
0.17 mm Hf			

VI. CONCLUSIONS

We have developed a noise-based analysis to study the merit of a detector that is segmented in the depth direction for quantitative bone absorptiometry and for “radiographic” imaging. The detector allows the x-ray absorption as a function of depth to be used for energy discrimination. Because of the additional information available as compared to front-back detectors which combine photons into only two groups, we hypothesized that this approach would lead to lower noise and a level of performance closer to that of the ideal energy discriminating detector. Somewhat surprisingly, this segmented detector adds little improvement to the gain that an inactive filter layer makes to a front-back detector if the spectrum contains photons of only two energies. In the case of a polychromatic beam, this multi-cell detector approximately doubles the benefit of the inactive filter layer. A more significant advantage over the front-back detector with a filter is that the improved performance is achieved without discarding any photons. This results in significantly improved performance for “radiographic” imaging.

The simulations presented here assumed the new detector was segmented into 100 equal thickness portions. This large number of segments was selected in order to examine the full potential benefit of depth segmentation. Clearly, most of the gain could be achieved with a much more modest design. For example, a detector in which the photons absorbed in the filter layer would be allowed to generate signal (i.e., three segments of unequal thickness), such as suggested by Ergun *et al.*,¹¹ would have performance comparable to the front-back detector with a filter for bone quantitation, and comparable to a system without the filter for “radiographic” imaging.

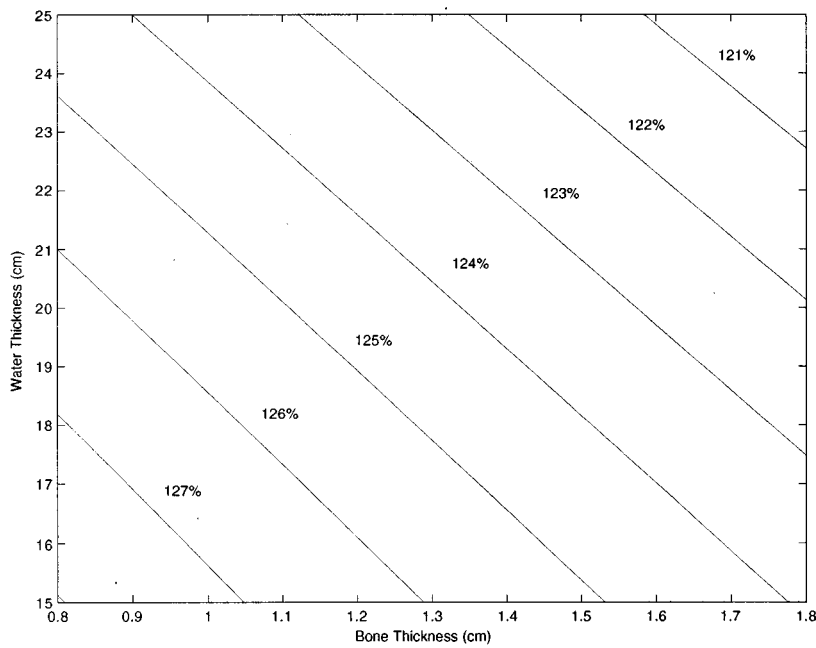


FIG. 5. Standard deviation in a single component image for a two cell detector relative to an ideal energy discriminating detector for a filtered 150 kVp beam. The numerical values on the plot correspond to the contour lines to the left of the numbers. A value of 100% indicates equal standard deviations for the two cell detector and the ideal detector.

ACKNOWLEDGMENTS

This research was supported in part by the National Institutes of Health, by Lunar Corporation (Madison, WI), and by the Lucas Foundation. The authors would like to thank Dr. Yudong Zhu for discussions regarding algorithm development. Portions of this paper were presented at the 1997 American Association of Physicists in Medicine Annual Meeting, and the 1997 Radiological Society of North America Annual Meeting. Send reprint requests to: Grant Stevens, Lucas MRSI Center, Stanford University MC 5488, Stanford, CA 94305.

APPENDIX: MORE THAN TWO ENERGY MEASUREMENTS

1. Single cell detector

In the case of a single cell, energy discriminating detector and a polychromatic beam, the energy signals are:

$$S_j = N_{0j} \alpha_j \eta_j e^{-\mu_{Bj} B - \mu_{Wj} W}, \quad j = 1, \dots, M, \quad (\text{A1})$$

where N_{0j} is the number of photons at energy E_j which are incident on the body, α_j has value E_j for an intensity-based detector and value 1 for a photon counting detector, η_j is the

detector efficiency at energy E_j , and M is the number of energy bins in the discretized spectrum. Log signals can be defined as:

$$L_j \equiv \ln \left(\frac{N_{0j} \alpha_j \eta_j}{S_j} \right) = \mu_{Bj} B + \mu_{Wj} W. \quad (\text{A2})$$

Because this system is overdetermined for quantitating bone, a weighted least squares technique can be used to solve for the amount of bone. A least squares statistic is defined as the weighted sum of the squared difference between the expected log signal at each energy [Eq. (A2)], and the measured log signal \tilde{L}_j :

$$\chi^2 = \sum_{j=1}^M (\mu_{Bj} B + \mu_{Wj} W - \tilde{L}_j)^2 w_j. \quad (\text{A3})$$

The optimal weights are the inverse of the log signal variances,¹⁶ where the variance in each signal S_j is $\alpha_j S_j$. Minimizing χ^2 [Eq. (A3)] with respect to the amount of bone and water yields the amount of bone:

$$B = \frac{(\sum_{j=1}^M \mu_{Wj}^2 w_j)(\sum_{j=1}^M \mu_{Bj} \tilde{L}_j w_j) - (\sum_{j=1}^M \mu_{Bj} \mu_{Wj} w_j)(\sum_{j=1}^M \mu_{Wj} \tilde{L}_j w_j)}{(\sum_{j=1}^M \mu_{Bj}^2 w_j)(\sum_{j=1}^M \mu_{Wj}^2 w_j) - (\sum_{j=1}^M \mu_{Bj} \mu_{Wj} w_j)^2}. \quad (\text{A4})$$

The expected noise in the bone can be calculated using propagation of errors:

$$\sigma_B^2 = \sum_{j=1}^M \left(\frac{\partial B}{\partial L_j} \right)^2 \left(\frac{\partial L_j}{\partial S_j} \right)^2 \sigma_{S_j}^2. \quad (\text{A5})$$

The expected variance in B is thus:

$$\sigma_B^2 = \sum_{n=1}^M \left[\frac{(\sum_{j=1}^M \mu_{Wj}^2 w_j) \mu_{Bn} - (\sum_{j=1}^M \mu_{Bj} \mu_{Wj} w_j) \mu_{Wn}}{(\sum_{j=1}^M \mu_{Bj}^2 w_j)(\sum_{j=1}^M \mu_{Wj}^2 w_j) - (\sum_{j=1}^M \mu_{Bj} \mu_{Wj} w_j)^2} \right]^2 \frac{\alpha_n w_n^2}{S_n}. \quad (A6)$$

2. Segmented detectors

The signal from each cell of a segmented detector (composed of K individual cells) used with a polychromatic beam can be approximated using effective attenuation coefficients. For each signal, a reference amount of bone and water is modified by attenuation through incremental thicknesses:

$$S_i = \left(\sum_{j=1}^M N_j^{\text{ref}} \alpha_j \eta_{ij} \right) e^{-\bar{\mu}_{Bi} \delta B - \bar{\mu}_{Wi} \delta W}, \quad i = 1, \dots, K, \quad (A7)$$

where effective attenuation coefficients for bone and water are defined as:

$$\bar{\mu}_{Bi} \equiv -\frac{\partial S_i}{\partial \delta B}, \quad \bar{\mu}_{Wi} \equiv -\frac{\partial S_i}{\partial \delta W}. \quad (A8)$$

Here, N_j^{ref} is the expected number of x-rays to penetrate through the reference amount of tissue and bone at energy

E_j , and M is the number of energy bins in the discretized x-ray spectrum. Log signals for each of the cells can be defined:

$$L_i \equiv \ln \left(\frac{\sum_{j=1}^M N_j^{\text{ref}} \alpha_j \eta_{ij}}{S_i} \right) = \bar{\mu}_{Bi} \delta B + \bar{\mu}_{Wi} \delta W. \quad (A9)$$

As before, this system is overdetermined for quantitating bone, and we use a weighted least squares technique to solve for the amount of bone. The least squares statistic is written:

$$\chi^2 = \sum_{i=1}^K (\bar{\mu}_{Bi} \delta B + \bar{\mu}_{Wi} \delta W - \tilde{L}_i)^2 w_i, \quad (A10)$$

where \tilde{L}_i is the measured log signal. Minimizing Eq. (A10) with respect to the amount of bone and water yields the amount of bone present:

$$\delta B = \frac{(\sum_{i=1}^K \bar{\mu}_{Wi}^2 w_i)(\sum_{i=1}^K \bar{\mu}_{Bi} L_i w_i) - (\sum_{i=1}^K \bar{\mu}_{Bi} \bar{\mu}_{Wi} w_i)(\sum_{i=1}^K \bar{\mu}_{Wi} L_i w_i)}{(\sum_{i=1}^K \bar{\mu}_{Bi}^2 w_i)(\sum_{i=1}^K \bar{\mu}_{Wi}^2 w_i) - (\sum_{i=1}^K \bar{\mu}_{Bi} \bar{\mu}_{Wi} w_i)^2}, \quad (A11)$$

where w_i is the inverse of the expected variance in each signal S_i , i.e., $w_i^{-1} = \sigma_{S_i}^2 = \sum_{j=1}^M N_j \alpha_j^2 \eta_{ij}$. The expected noise in the bone can be calculated using propagation of errors:

$$\sigma_B^2 = \sum_{i=1}^K \left(\frac{\partial B}{\partial L_i} \right)^2 \left(\frac{\partial L_i}{\partial S_i} \right)^2 \sigma_{S_i}^2. \quad (A12)$$

This yields:

$$\sigma_B^2 = \sum_{n=1}^K \left[\frac{(\sum_{i=1}^K \bar{\mu}_{Wi}^2 w_i) \bar{\mu}_{Bn} - (\sum_{i=1}^K \bar{\mu}_{Bi} \bar{\mu}_{Wi} w_i) \bar{\mu}_{Wn}}{(\sum_{i=1}^K \bar{\mu}_{Bi}^2 w_i)(\sum_{i=1}^K \bar{\mu}_{Wi}^2 w_i) - (\sum_{i=1}^K \bar{\mu}_{Bi} \bar{\mu}_{Wi} w_i)^2} \right]^2 \frac{w_n^2}{S_n^2} \sum_{j=1}^M N_j \alpha_j^2 \eta_{nj}. \quad (A13)$$

¹L. A. Lehmann, R. E. Alvarez, A. Macovski, W. R. Brody, N. J. Pelc, S. J. Riederer, and A. L. Hall, "Generalized image combinations in dual kVp digital radiography," *Med. Phys.* **8**, 659–667 (1981).

²L. T. Niklason, N. M. Hickey, D. P. Chakraborty, E. A. Sabbagh, M. V. Yester, R. G. Fraser, and G. T. Barnes, "Simulated pulmonary nodules: Detection with dual-energy digital versus conventional radiography," *Radiology* **160**, 589–593 (1986).

³T. Asaga, S. Chiyasu, S. Mastuda, H. Mastuura, H. Kato, M. Ishida, and T. Komaki, "Breast imaging: Dual-energy projection radiography with digital radiography," *Radiology* **164**, 869–870 (1987).

⁴D. T. Baran, K. G. Faulkner, H. K. Genant, P. D. Miller, and R. Pacifici, "Diagnosis and management of osteoporosis: Guidelines for the utilization of bone densitometry," *Calcif. Tissue Int.* **61**, 433–440 (1997).

⁵S. L. Silverman, "Calcitonin," *Am. J. Med. Sci.* **313**, 13–16 (1997).

⁶U. A. Liberman *et al.*, "Effect of oral alendronate on bone mineral density and the incidence of fractures in postmenopausal osteoporosis," *N. Engl. J. Med.* **333**, 1437–1443 (1995).

⁷A. A. Licata, "Bisphosphonate therapy," *Am. J. Med. Sci.* **313**, 17–22 (1997).

⁸J. A. Sorenson, P. R. Duke, and S. W. Smith, "Simulation studies of dual-energy x-ray absorptiometry," *Med. Phys.* **16**, 75–80 (1989).

⁹G. T. Barnes, R. A. Sones, M. M. Tesic, D. R. Morgan, and J. N. Sanders, "Detector for dual-energy digital radiography," *Med. Phys.* **156**, 537–540 (1985).

¹⁰H. N. Cardinal and A. Fenster, "Theoretical optimization of a split septaless xenon ionization detector for dual-energy chest radiography," *Med. Phys.* **15**, 167–180 (1988).

¹¹D. L. Ergun, C. A. Mistretta, D. E. Brown, R. T. Bystrianyk, W. K. Sze, F. Kelcz, and D. P. Naidich, "Single-exposure dual-energy computed

- radiography: Improved detection and processing," *Radiology* **174**, 243–249 (1990).
- ¹²D. R. Morgan, R. A. Sones, and G. T. Barnes, "Performance characteristics of a dual-energy detector for digital scan projection radiography," *Med. Phys.* **14**, 728–735 (1987).
- ¹³D. M. Gauntt and G. T. Barnes, "X-ray tube potential, filtration, and detector considerations in dual-energy chest radiography," *Med. Phys.* **21**, 203–218 (1994).
- ¹⁴D. P. Chakraborty and G. T. Barnes, "An energy sensitive cassette for dual-energy mammography," *Med. Phys.* **16**, 7–13 (1989).
- ¹⁵F. Kelcz, P. M. Joseph, and S. K. Hilal, "Noise considerations in dual energy CT scanning," *Med. Phys.* **6**, 418–425 (1979).
- ¹⁶J. Mandel, *The Statistical Analysis of Experimental Data* (Dover, New York, 1964).
- ¹⁷National Institute of Standards and Technology, "<http://physics.nist.gov/PhysRefData/XrayMassCoef/tab3.html>," website.
- ¹⁸National Institute of Standards and Technology, "<http://physics.nist.gov/PhysRefData/XrayMassCoef/tab2.html>," website.
- ¹⁹H. E. Johns and J. R. Cunningham, *The Physics of Radiology* (Thomas, Springfield, IL, 1983).
- ²⁰E. Storm *et al.*, "Calculated Bremsstrahlung spectra from thick tungsten targets," *Phys. Rev. A* **5**, 2328–2338 (1972).
- ²¹N. A. Dyson, *X-Rays in Atomic and Nuclear Physics* (Longman, London, 1973).